7-2021

Uranium Integral Fission Product Yields for a Spectrally-shaped 14.1 MeV Neutron Source at the National Ignition Facility

Nicholas J. Quartemont

N. Gharibyan

K. Moody

James E. Bevins
Air Force Institute of Technology

Recommended Citation

Quartemont, N., Gharibyan, N., Moody, K., & Bevins, J. E. (2021). Uranium integral fission product yields for a spectrally-shaped 14.1 MeV neutron source at the National Ignition Facility. Applied Radiation and Isotopes, 173, 109711. https://doi.org/10.1016/j.apradiso.2021.109711

Applied Radiation and Isotopes 173 (2021) 109711

Contents lists available at ScienceDirect

Applied Radiation and Isotopes

journal homepage: www.elsevier.com/locate/apradiso

Uranium integral fission product yields for a spectrally-shaped 14.1 MeV neutron source at the National Ignition Facility

N. Quartemont [a,*], N. Gharibyan [b], K. Moody [b], J.E. Bevins [a]

[a] Department of Engineering Physics, Air Force Institute of Technology, WPAFB, OH, 45433, USA
[b] Lawrence Livermore National Laboratory, Livermore, CA, 94550, USA

ARTICLE INFO

Keywords:
Neutron energy tuning
Spectrum unfolding
Activation foils
Integrated fission product yields

ABSTRACT

This paper describes the experimental results for an energy tuning assembly created to modify the National Ignition Facility deuterium–tritium fusion neutron source into a notional thermonuclear and prompt fission neutron spectrum, which has applications in integral measurements, nuclear data benchmarks, and radiation effects on microelectronics. The Monte Carlo neutron transport utilized MCNP5 to estimate the ETA-modified fluence using the ENDF-B/VIII.0 and IRDFF-II continuous energy nuclear data libraries, and SCALE Sampler was used to estimate the systematic nuclear data covariance using ENDF-B/VII.1 and IRDFF-II in a 252-group structure. The experiment fielded eight activation foils and a highly enriched uranium sample. This provided fifteen reaction channels that were used in a forward-fit comparison to the modeled results and to unfold the neutron spectrum using STAYSL. Gamma-ray spectrometry was performed on the activation and highly enriched uranium foils, and the reduced χ^2 between the modeled and experimental values was 1.21. The results from the STAYSL unfold, reduced $\chi^2 = 1.62$, indicated that the modeled neutron spectrum was achieved and the systematic nuclear data uncertainty associated with the neutron transport and activation product cross sections was representative of the experiment. Integral cumulative fission product yield data were collected for 37 mass chains with a combination of gamma-ray spectrometry and radiochemical analysis. Fission product analysis was generally in agreement with two models using a semi-empirical fit and the General Observables of Fission code, with the exception of mass chains 88, 109, 111, 112, 113, 129, 139, 142, 144, 151, and 156.

1. Introduction

An energy tuning assembly (ETA) experiment was performed at the National Ignition Facility (NIF) to spectrally shape the deuterium–tritium (D-T) 14.1 MeV fusion neutron spectrum into a modified thermonuclear (TN) and prompt fission neutron spectrum (PFNS). Customizable neutron environments offer increased access to unique neutron energy spectra, which can provide data on integral measurement needs and activation dosimetry validation (Bernstein et al., 2019; Trkov et al., 2020). Many testing facilities targeting integral measurements focus on nuclear reactor spectra, the Watt fission spectrum, and the 14.1 MeV D-T fusion process. Accelerators can also provide a nearly mono-energetic neutron source for discrete energy measurements (Gooden et al., 2016).

Utilizing different neutron spectra can identify nuclear data gaps and inaccurate evaluations that feed into nuclear data libraries used in modern radiation transport simulations (Kahler et al., 2014). In particular, integral fission product yield (IFY) measurements inform nuclear data libraries and models, which are essential knowledge for nuclear reactor operations, international nuclear treaty monitoring, and technical nuclear forensics. The NIF has a unique capability as a high-density D-T prompt neutron source that can be used to produce nearly instantaneous fission products under the appropriate neutron spectrum distribution without any saturation or decay effects common with nuclear reactor or accelerator production. The ETA, or similar platform, could also be utilized to study radiation effects on electronics and create environments for nuclear data benchmarks.

The ETA design Bevins (2017) considered in this work was previously tested at the Lawrence Berkeley National Laboratory (LBNL) 88-Inch Cyclotron to validate initial modeling concepts and neutron spectrometry techniques (Bevins et al., 2019). The modeling of the expected experimental outcomes and uncertainties was improved by accounting for nuclear data covariance analysis, which improved the quality of the foil activation spectrometry used to measure the ETA-generated neutron environment (Quartemont et al., 2020b).

This work describes the first ETA experimental results from the NIF to generate a TN+PFNS neutron environment. The experimental design,

* Corresponding author.
E-mail address: nicholas.quartemont@afit.edu (N. Quartemont).

https://doi.org/10.1016/j.apradiso.2021.109711
Received 19 October 2020; Received in revised form 23 March 2021; Accepted 25 March 2021
Available online 3 April 2021

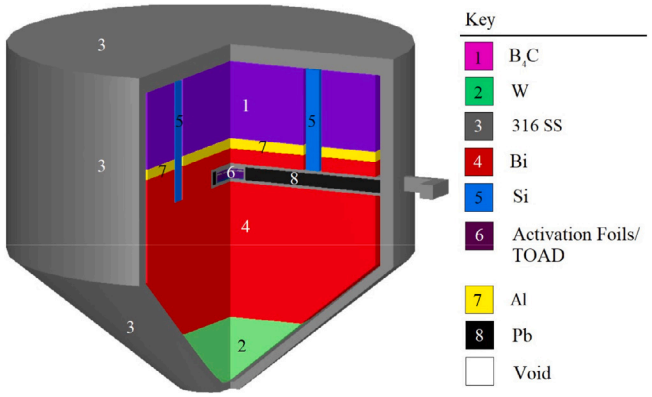

Fig. 1. (Color online) The ETA designed to achieve the TN+PFNS via spectral modification of the NIF neutron source.

modeling, and results from activation analysis and the unfolding of the neutron fluence with Pacific Northwest National Laboratory's (PNNL's) STAYSL Rearden and Jessee (2013) are described. Finally, results of 47 cumulative and independent IFY across 37 mass chains for a highly enriched uranium sample are presented.

2. Experiment

The ETA, shown in Fig. 1, was designed to produce a notional thermonuclear and prompt fission neutron spectrum (TN+PFNS) relevant to the production of surrogate post-detonation weapon debris (Bevins et al., 2019). The ETA design is 28 cm in diameter and approximately 24 cm in height. The ETA consists of cones and cylinders of boron carbide, aluminum, bismuth, tungsten, silicon, 316 stainless steel, and lead. Each ETA part is manufactured with three or four nines pure material and sub-mm tolerances thereby limiting sources of systematic uncertainty.

The ETA was fielded with an activation foil pack and a HEU foil placed in the sample cavity, item 6 in Fig. 1, where the objective TN+PFNS neutron spectrum was achieved. ETA was fielded with eight activation foils, summarized in Table 1. Each activation foil had a radius of 2.5 cm with the exception of manganese and the HEU. The manganese foil was a 2.5 cm side length square foil. The HEU (93.217 w/o) utilized for the experiment consisted of three disk samples (HEU1, HEU2, and HEU3) weighing 0.3675, 0.3549, and 0.3550 g with a maximum weight uncertainty of 0.2% with areas of 4.99, 4.72, and 4.88 cm^2. The HEU samples were encased in a hermetically sealed Target Option Activation Device (TOAD) (Gharibyan et al., 2015). The TOAD was positioned between indium and tungsten as depicted in Table 1.

The NIF source for shot N191020_001 was located 15 cm below the base of the cone and was a D-T Polar Drive Exploding Pusher (PDXP) target (Ellison et al., 2018). The source configuration utilized a 64/36 D-T mix capsule with a 1.44 mg mass, 29 μm thick, and 4.05 mm outer diameter. The PDXP shot delivered 1.56 MJ of laser energy, enabling thermonuclear fusion with a nominal yield of $1.08 \pm 0.04 \times 10^{16}$ neutrons over 424 ps with a minimum plasma ion temperature of 8.36 keV (Yeamans and Bleuel, 2017). The ETA experiment was fielded on a Target and Diagnostic Manipulator (TANDM) as an additional experiment to the Energetic Neutron Platform (ENP). The ETA, ENP, and target positioner (TARPOS) experimental configuration is shown in Fig. 2.

3. Analysis methods

The primary analysis techniques utilized in this work were Monte Carlo simulation, gamma-ray spectrometry, modeling of fission products, neutron spectrum unfolding, and radiochemistry. The modeled

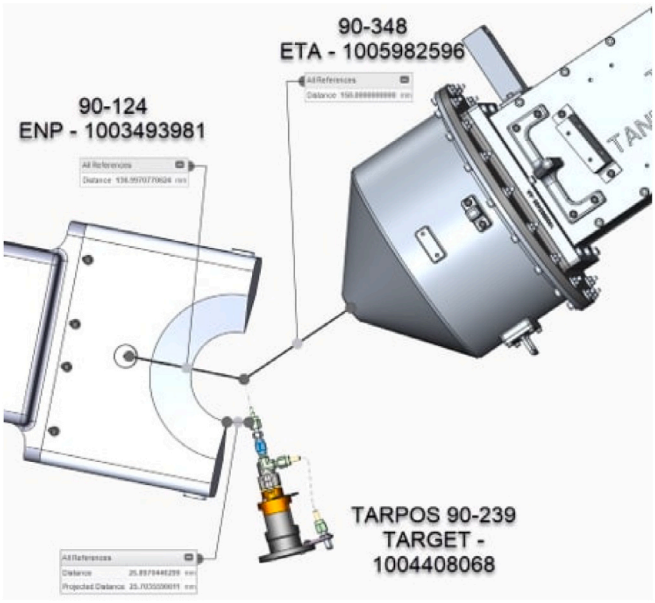

Fig. 2. (Color online) NIF chamber experimental configuration of TARPOS, ENP, and ETA.

neutron environment with MCNP and SCALE was used to predict the neutron environment and resulting observable products such as activation or fission products (Rearden and Jessee, 2018; X-5 Monte Carlo Team, 2008). Experimental measurements of the products included gamma-ray spectroscopy and radiochemistry on the fission products. The primary codes and data utilized are summarized in Table 2. A repository containing the primary model inputs and outputs utilized in this work can be accessed here (Quartemont, 2021).

3.1. Monte Carlo simulation

The ETA neutronics design was modeled in MCNP5 to determine the expected neutron environment in the sample cavity and in SCALE MAVRIC with Sampler to propagate nuclear data covariance in the transport model (Rearden and Jessee, 2018; X-5 Monte Carlo Team, 2008). MCNP5 was used for continuous energy (CE) MC neutron transport and to benchmark MC neutron transport in CE SCALE MAVRIC. The MAVRIC MC simulation was then used in a 252 energy group structure with the SCALE Sampler module to assess the effect of nuclear data covariance through stochastic sampling of the ENDF-B/VII.1 nuclear data library (Chadwick et al., 2011). Finally, the activation foil covariances were sampled with a multivariate normal distribution to incorporate the reaction cross-section uncertainty with an interpolation scheme described with the IRDFF-II nuclear data library (Trkov et al., 2020). Previous work has described the methodology in detail to characterize the effect of nuclear data covariance for NIF ETA simulations (Quartemont et al., 2020b,a).

The MCNP5 ETA model was created with a surface source read (SSR) file generated using a neutron point source with a mean energy of 14.07 MeV (Appelbe and Chittenden, 2014). The SSR, a box around ETA, was made with a validated full-scale NIF model including the TARPOS, ETA, TANDM (90-348), snout diagnostic instrument manipulator (DIM), Sandia ENP experiment, TANDM (90-124), and target chamber support structures and used the ENDF/B-VII.1 library (Chadwick et al., 2011). Time dependence in the neutron source was neglected because NIF neutron emission generations are approximately 300 picoseconds (Yeamans and Bleuel, 2017). The ENDF/B-VIII.0 nuclear data library was used for the neutron transport inside the SSR

Table 1
Summary of activation foils and reactions selected to unfold the neutron energy spectrum. The order of the foils was in the listed order with Au-1 closest to the NIF source.

Foil (Thickness)	Mass [g]	Reaction [IRDFF v.1.05 Reaction Number]	Threshold [MeV] (@ 10 mb)	Primary Radiation [keV] (Intensity)	$t_{1/2}$	Decay Data
Au-1 (0.09 mm)	3.718	^{197}Au (n,2n) ^{196}Au^{g+m1} [16]	8.1 (8.3)	355.7 (0.87)	6.17 days	(Xiaolong, 2007)
		^{197}Au (n,g) ^{198}Au [102]	Thermal	411.8 (0.9562)	2.69 days	(Huang and Kang, 2016)
Zr (0.97 mm)	12.683	^{90}Zr (n,2n) ^{89}Zr [16]	12.1 (12.1)	909.2 (0.9904)	78.41 h	Singh (2013)
Mn (1.12 mm)	5.028	^{55}Mn (n,2n) ^{54}Mn [16]	10.4 (10.6)	834.85 (0.99976)	312.2 days	(Dong and Junde, 2014)
		^{55}Mn (n,g) ^{56}Mn [102]	Thermal	846.8 (0.9885)	2.58 h	(Junde et al., 2011)
In (1.03 mm)	14.811	^{113}In (n,n') ^{116}In^{m1} [11004]	0.4 (0.7)	391.7 (0.6494)	99.5 min	(Blachot, 2010a)
		^{115}In (n,n') ^{116}In^{m1} [11004]	0.3 (0.6)	336.24 (0.459)	4.49 h	(Blachot, 2012)
		^{115}In (n,g) ^{116}In^{m1} [11102]	Thermal	1293.56 (0.848)	54.29 min	(Blachot, 2010b)
HEU (0.12 mm)	1.0774	^{238}U (n,g) ^{239}Np [102]	Thermal	106.36 (0.202)	2.356 days	Browne and Tuli (2015)
W (1.02 mm)	37.964	^{186}W (n,g) ^{187}W [102]	Thermal	685.51 (0.332)	24 h	(Basunia, 2009)
Ni (1.12 mm)	14.316	^{58}Ni (n,2n) ^{57}Ni [16]	12.4 (13.3)	1378 (0.817)	35.6 h	(Bhat, 1998)
		^{58}Ni (n,p) ^{58}Co^{g+m1} [103]	0 (1.3)	810.8 (0.9945)	70.86 days	(Nesaraja et al., 2010)
Al (1 mm)	5.428	^{27}Al (n,a) ^{24}Na [107]	3.2 (6.7)	1368.63 (0.9999)	15 h	(Firestone, 2007)
Au-2 (0.09 mm)	3.692	^{197}Au (n,2n) ^{196}Au^{g+m1} [16]	8.1 (8.3)	355.7 (0.87)	6.17 days	(Xiaolong, 2007)
		^{197}Au (n,g) ^{198}Au [102]	Thermal	411.8 (0.9562)	2.69 days	(Huang and Kang, 2016)

source, and the IRDFF-II library was used for the activation cross-sections Brown et al. (2018). The difference in transport libraries after the SSR was created was a limitation of NIF-validated model.

A lower fidelity SCALE MAVRIC model was also created for the experimental setup of the NIF. The MAVRIC model with Sampler included a full fidelity model of ETA and representative geometry for the remainder. The source specifications were identical to MCNP5; however, only the ENDF/B-VII.1 library was available in SCALE (Rearden and Jessee, 2018). The results from 285 samples in Sampler running MAVRIC in the 252-group structure were characterized with statistical bootstrapping to determine a 1-σ uncertainty in the reaction products and fluence distribution. The Sampler transport uncertainty and flux correlation matrix are shown in Fig. 3.

The resulting correlation matrix and uncertainty were used in the unfolding routine in STAYSL to bound the possible outcome. The correlation matrix indicated nearby energy group correlations and an anti-correlation between the TN neutrons near 14 MeV and peak of the PFNS near 1 MeV because removal mechanisms – such as (n,2n) and (n,n') – in the TN region are needed to populate the PFNS. The associated neutron fluence uncertainty was 5.3% at 14.1 MeV, due to the uncertainty in tungsten and bismuth attenuation coefficients. The uncertainty at 1 MeV was 2.9% because there are multiple paths to down-scatter the source neutrons, including spallation (n,2n) reactions primarily on W and Bi components in addition to successive inelastic scattering events. At 1.3 eV, the uncertainty reached 67% due to the large number of interactions required to moderate a D-T neutrons to low energy. The low energy neutron distribution is not well described by a normal distribution, and this creates a limitation of assumed normally distributed uncertainties in STAYSL at low energy (Taavitsainen and Vanhanen, 2017).

3.2. Activation analysis

Activation analysis was performed with gamma-ray spectrometry using three high purity germanium (HPGe) and multi-channel analyzer systems in the LLNL counting facility on the activation foils and HEU1 sample (Gharibyan et al., 2015). Two methods were performed to analyze the energy dependent counts, GAMANAL, which was created for analysis of fission product spectra, and PeakEasy 4.97, which was also used for peak fitting (Gunnink and Niday, 1972). The fission product nuclear data utilized in this analysis was from literature, the Table of Isotopes, 8th Edition and data retrieved from the National Nuclear Data Center Chart of the Nuclides Online Data Service (Firestone,

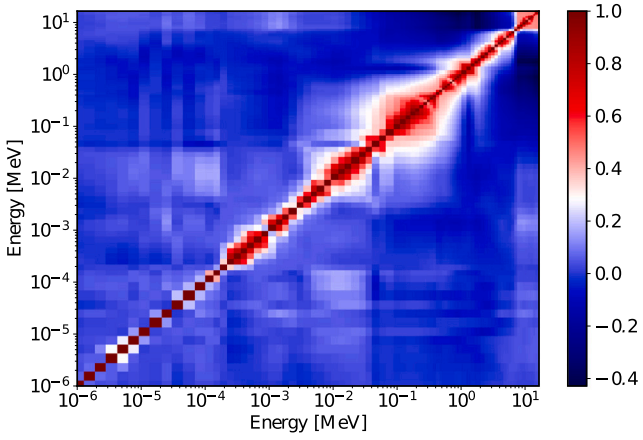

(a) Correlation matrix

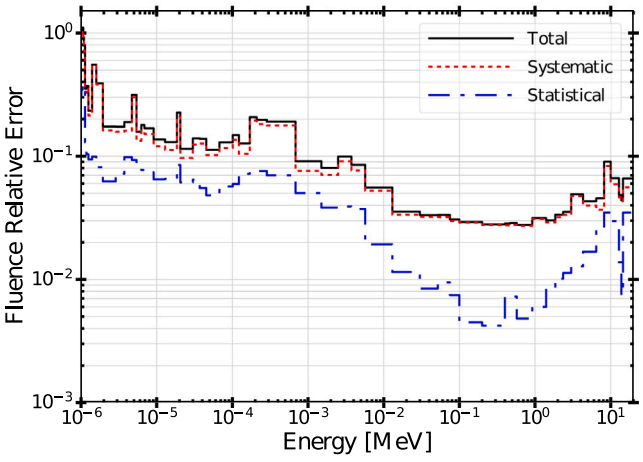

(b) Relative Uncertainty

Fig. 3. (Color online) Neutron fluence covariance parameters in ETA sample cavity showing the (a) correlation matrix and (b) relative statistical and systematic uncertainty as a function of energy.

Table 2
Primary codes and methods utilized.

Purpose	Code/Method (Library)
Monte Carlo Neutron Transport	MCNP5 (ENDF/B-VII.1 and ENDF/B-VIII.0)
	SCALE MAVRIC and Sampler (ENDF/V-VII.1 252-group)
Gamma-ray Spectrometry	GAMANAL
	PeakEasy 4.97
Fission Product Estimation	GEF
	Semi-empirical fits
Neutron Flux Spectrum Unfolding	PNNL STAYSL (IRDFF v.1.05 129-group)

1996). GAMANAL was calibrated with standard calibration sources to determine the efficiency as a function of sample position, energy, and detector geometry. GAMANAL performed gamma-ray attenuation corrections and counting of peaks using multiple linear regression least squares with smoothed Gaussian peak fits (Gunnink and Niday, 1972).

Measurements of the activity were decay corrected to the reaction product atoms (N_0) immediately after irradiation by

$$N_0 = \frac{(C - B)e^{\lambda t_d}}{\epsilon(1 - e^{-\lambda t_c})I_\gamma}, \quad (1)$$

where the measured counts (C) were reduced by the background counts (B) and corrected for decay between the end of irradiation and the start of counting (t_d). A correction factor was used for radioactive decay during counting time (t_c). The detector efficiency for the given gamma-ray energy (ϵ) was determined with GAMANAL to include gamma-ray self-shielding. Finally, the relative gamma intensity (I_γ) for each decay was taken into account.

Each foil was counted until approximately 10,000 counts were detected from the reaction products. All reactions did not require in-growth corrections, with the exception of the $^{196}Au^{g+m1}$ reaction product. The $^{58}Co^{m1}$ reaction product is not suitable for gamma-ray spectrometry, so the sample was allowed to decay for two weeks prior to the measurement of $^{58}Co^{g+m1}$. Similarly, ^{239}Np was measured after the short-lived decay of ^{239}U.

A variance-based weighted average was taken for each decay gamma ray associated with a product nuclei for each measurement of that decay mode (Moody et al., 2020). The final weighted average of each gamma-ray decay mode measurement was then done to determine N_0 for each product. Radioactive decay uncertainties were added after accounting for the statistical error and a 2% system systematic error (Moody et al., 2020). Uncertainties associated with the weight and size of the activation foils were neglected as negligible in this work with respect to the measurement uncertainty.

3.3. Fission product models

The modeled neutron fluence was convolved with the fission cross section to produce the expected experimental fission product production from ^{235}U and ^{238}U with two techniques. First, the energy spectrum of neutrons causing fission was used to determine the fission product yield with a phenomenological fit and the General Description of Fission Observables (GEF) code (Schmidt et al., 2016). Second, semi-empirical relations developed by Nagy et al. were used to predict the fission product yield as a function of energy given sufficient yield-dependent fission product measurement data (Nagy et al., 1978).

GEF is applicable over a wide range of fissioning systems, including isotopes with atomic numbers from 80 to 112 (Schmidt et al., 2016). GEF incorporates covariance information of the fissioning system, multi-chance fission, and many other unique features. The values for the mass chain yield distribution calculated by GEF were determined using separate calculations for each energy group defined by the midpoint bin energy of the fissioning system, ^{236}U for neutron-induced ^{235}U fission and ^{239}U for neutron-induced ^{238}U fission. The uncertainty reported in this work includes GEF statistical, GEF systematic covariance, and the Sampler systematic uncertainty for the fissioning neutron energy distribution.

The semi-empirical formula for estimating fission product yield is given by

$$Y(E_n) = Y_0 e^{bE_n}, \quad (2)$$

where the fitting parameters b and Y_0 represent the slope of the function in logarithmic form and thermal fission yield, respectively (Nagy et al., 1978). The slope is the primary measure of the energy dependence of the fission product yield, which requires modifications for multi-chance fission. First chance fission is dominant from up to 5.5 MeV and second-chance fission up to 14.1 MeV Nagy et al. (1978), requiring modifications to incorporate first and second chance fission in this work. Correlations between fission product yield as a function of energy were not captured because data were not available.

The measured fission products were compared through relative fission yields, R values (Selby et al., 2010). The R value was used to remove unknown systematic errors and is a ratio given by

$$R = \frac{A_i^{f,e} \Big/ A_{97}^{f,e}}{A_i^* \Big/ A_{97}^*} = \frac{N_i^{f,e} \Big/ N_{97}^{f,e}}{N_i^* \Big/ N_{97}^*} = \frac{N_i^{f,e} \Big/ N_{97}^{f,e}}{Y_i^* \Big/ Y_{97}^*}, \quad (3)$$

where the activity ratio between the ith measured fission product or mass chain time-corrected atoms ($N_i^{f,e}$) to the measured $A = 97$ mass chain atoms ($N_{97}^{f,e}$) was normalized by the ENDF-B/VIII.0 ^{235}U thermal fission product yield ratio of the ith fission product mass chain (Y_i^*) to the yield for the $A = 97$ mass chain (Y_{97}^*). The $A = 97$ mass chain was chosen because ^{97}Zr provided a strong gamma-ray for measurement and is a well-characterized peak fission product.

3.4. Neutron spectrum unfolding

The measured foil activation products were used with an average foil pack MCNP5 CE fluence and SCALE Sampler neutron fluence covariance to unfold the neutron spectrum using STAYSL with the IRDFF v.1.05 129-energy group structure. The most current version of STAYSL did not include IRDFF-II, where the reaction cross-section and covariance matrix for $^{197}Au(n, \gamma)$ and $^{238}U(n, \gamma)$ were updated. The 129-group cross-section library was derived for D-T neutron experiments; however, the cross-section integrating function results in increased radiative capture reactions compared to the CE solution. For example, the $^{197}Au(n, \gamma)$ was 29% higher and $^{186}W(n, \gamma)$ was 53% higher in the 129-group STAYSL library than the CE solution. The STAYSL (n, γ) microscopic cross-sections were re-calculated with MCNP5 with IRDFF-II data in the 129-group STAYSL structure to correct the cross section integrating function. This allowed the use of IRDFF-II $^{197}Au(n, \gamma)$ and $^{238}U(n, \gamma)$ reaction cross-sections in STAYSL. However, the IRDFF v.1.05 covariance matrices for $^{197}Au(n, \gamma)$ and $^{238}U(n, \gamma)$ were still used. The 129-group cross-sections are shown in Fig. 4.

MCNP5 was used to generate energy-dependent neutron self-shielding factors to account for attenuation within and across the foil pack in a mixed neutron field and beam environment similar to other thick-foil techniques (Vagena et al., 2018). The self-shielding factors were required for modification of the neutron flux throughout the foil pack due to the relatively large size of the foils used resulting in non-negligible attenuation as shown in Fig. 5.

STAYSL determines the incident neutron flux using a generalized least-squares spectral adjustment based on a χ^2 comparison of the measured activation products and the activities calculated from an

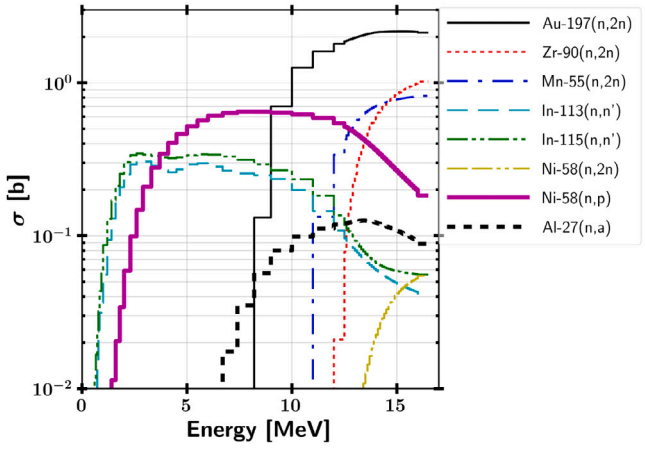

(a) Threshold reactions

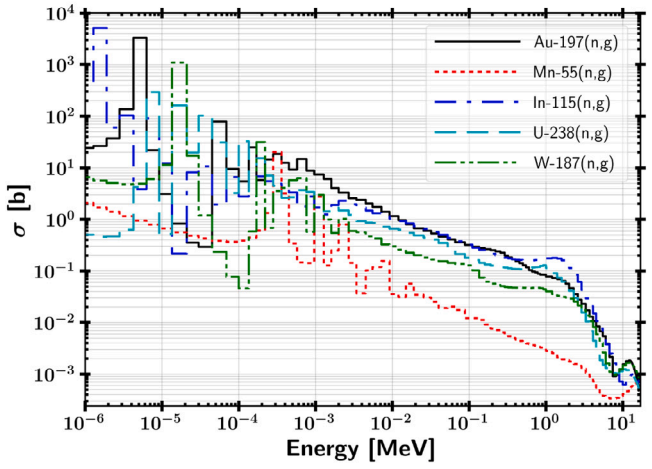

(b) Thermal reactions

Fig. 4. (Color online) Neutron activation cross-sections used in STAYSL for the (a) threshold and (b) thermal reactions. The reaction cross sections indicate coverage of the energy range of interest with unique and overlapping measurements.

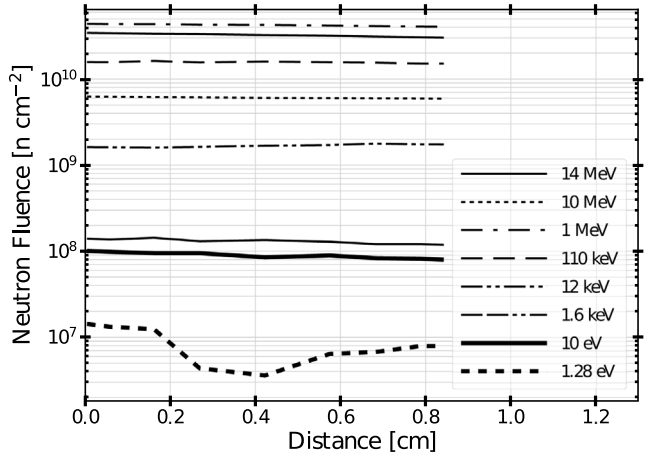

Fig. 5. Neutron fluence in ETA sample cavity showing exponential attenuation at high energy and nuclear resonance self-shielding at low energies.

adjusted flux (Greenwood and Johnson, 2016). The activity information ($A°$), a neutron flux, a nuclear data matrix (P), and covariance matrices are used in the formulation of the χ^2 statistic. The χ^2 is minimized based on the STAYSL minimized activity information ($\bar{A}$) and the STAYSL calculated neutron flux convolved with the IRDFF nuclear data parameters ($\bar{P}$). The χ^2 statistic utilized in STAYSL is given by

$$\chi^2 = \begin{bmatrix} P-\bar{P} \\ A°-\bar{A} \end{bmatrix}^{\dagger} \cdot \begin{bmatrix} N_P & 0 \\ 0 & N_{A°} \end{bmatrix}^{-1} \cdot \begin{bmatrix} P-\bar{P} \\ A°-\bar{A} \end{bmatrix} \quad (4)$$

where N_P is the covariance matrix from the flux and nuclear data and $N_{A°}$ is the activity covariance matrix (Perey, 1977).

Additionally, STAYSL requires an initial guess spectrum as the activities produced for the foils are often degenerate with multiple creation environments. However, the initial spectrum allows for a physics- and modeling-based result to guide the overall result. The initial guess spectrum was created with the mean value from MCNP5 over the entire activation foil pack volume and a neutron fluence covariance matrix as derived with Sampler (Quartemont et al., 2020b). The 252-group Sampler covariance matrix was mapped to the 129-group STAYSL structure through linear interpolation of the systematic uncertainties and correlation based on the midpoint of the energy bins for each structure.

3.5. Radiochemistry

Radiochemistry was performed to separate lower yield fission products that would not be observed in the bulk sample with gamma-ray spectrometry. Radiochemistry procedures were adopted from standard fission-product separation procedures found in their respective radiochemistry chapters and commonly utilized distribution tables (Hogdahl, 1961; Sunderman and Townley, 1961; DeVoe, 1960; Faris and Warton, 1962). The radiochemical procedures of HEU2 included dissolution in 9M HCl with 8M HNO_3 to remove the rare-earth (RE) fission products from the bulk HEU and subsequent separations to isolate desired elements (Gharibyan et al., 2018). A mixed lanthanide-yttrium RE carrier and aliquots of barium and cesium were added to HEU2 for chemical yielding and improved chemical performance. Additionally, a ^{237}Np tracer was added for yielding of ^{239}Np.

The neptunium fraction was eluted from an anion-exchange column. The RE fission products were separated into three fractions containing the light (La-Pr), medium (Nd-Pm) and heavy (Sm-Tb, containing Y) fractions after elution with a mixture of HNO_3 and methanol from an anion-exchange column. The dried fractions were dissolved in 10 ml of water, transferred to Prindle gamma-spec vials (cylindrical plastic vial with 10 cm^2 area), and analyzed with gamma-ray spectrometry. The fractions were counted on coaxial and planar HPGe detectors and evaluated by the GAMANAL code as described in Section 3.2 with decay-curve analysis to verify the half-life of the fission-product measurement. Chemical yielding was performed with inductively-coupled plasma mass spectroscopy (ICP-MS), where the tracer isotope concentration was used to determine chemical efficiency during separations for the measured radioisotopes.

Separations were performed on HEU3 after dissolution with the addition of palladium, cadmium, and silver carriers. An Ag_2S precipitate was formed to recover the silver fraction, and the palladium fraction was recovered with Pd-dimethylglyoxime precipitation. The cadmium fraction was taken after precipitation of uranium hydroxide as the effluent with an anion-exchange column. Each sample was collected in a Prindle vial and analyzed with gamma-ray spectrometry. An aliquot from each sample (Ag/Pd/Cd) along with a separate set of carrier solutions representing 100% yield were used for ICP-MS measurements to determine chemical recovery yields with yielding uncertainty from repeated sampling. The total uncertainty for the measured fission products includes nuclear data uncertainty in $t_{1/2}$ and γ-ray intensities, counting statistics, chemical recovery uncertainty, and weighted averaging for repeated measurements.

Table 3
Activation product measurements compared to modeled values.

Reaction Product	GAMANAL	Peak Easy	Experiment Average	Modeled
$^{196}Au^{g+m1}$	5.74E+9 ± 3.57%	5.75E+9 ± 3.67%	5.75E+9 ± 3.62%	5.85E+9 ± 4.48%
^{198}Au	2.24E+9 ± 2.01%	2.25E+9 ± 2.03%	2.25E+9 ± 2.02%	2.27E+9 ± 3.64%
^{89}Zr	5.81E+9 ± 2.02%	5.83E+9 ± 2.03%	5.82E+9 ± 2.03%	5.96E+9 ± 4.43%
^{54}Mn	8.65E+9 ± 3.82%	8.65E+9 ± 3.55%	8.65E+9 ± 3.69%	9.24E+9 ± 4.52%
^{56}Mn	3.33E+8 ± 2.12%	3.33E+8 ± 2.06%	3.25E+8 ± 2.09%	4.20E+8 ± 11.79%
$^{116}In^{m1}$	4.50E+8 ± 2.74%	4.50E+8 ± 2.70%	4.49E+8 ± 2.72%	4.46E+8 ± 2.11%
$^{116}In^{m1}$	1.18E+10 ± 5.40%	1.16E+10 ± 5.43%	1.17E+10 ± 5.42%	1.22E+10 ± 2.38%
$^{116}In^{m1}$	1.76E+10 ± 2.35%	1.83E+10 ± 3.06%	1.80E+10 ± 2.71%	1.70E+10 ± 3.41%
^{239}Np (Radiochemistry)	6.77E+6 ± 5.09%	N/A	6.77E+7 ± 5.09%	7.99E+6 ± 3.80%
^{187}W	2.41E+9 ± 2.53%	2.49E+9 ± 3.17%	2.45E+9 ± 2.85%	2.39E+9 ± 3.43%
^{57}Ni	5.55E+8 ± 3.39%	5.85E+8 ± 5.28%	5.70E+8 ± 4.34%	5.65E+8 ± 4.53%
$^{58}Co^{g+m1}$	1.63E+10 ± 2.04%	1.65E+10 ± 2.05%	1.64E+10 ± 2.05%	1.88E+10 ± 2.53%
^{24}Na	3.33E+9 ± 2.35%	3.40E+9 ± 2.06%	3.37E+9 ± 2.21%	3.34E+9 ± 4.34%
$^{196}Au^{g+m1}$	5.00E+9 ± 3.57%	5.05E+9 ± 3.67%	5.03E+9 ± 3.62%	5.15E+9 ± 4.46%
^{198}Au	2.01E+9 ± 2.01%	2.03E+9 ± 2.02%	2.02E+9 ± 2.02%	2.03E+9 ± 2.73%
χ^2/ν = 2.31 (excluding $^{58}Co^{g+m1}$ = 1.21)				

4. Results and discussion

4.1. Activation foils

The decay-corrected activation products compared to the modeled results and the χ^2 per degree of freedom (ν) are summarized in Table 3. The individual χ^2 contribution for a reaction included both modeled and measurement uncertainty added in quadrature. The experiment average activation product measurement is an average of the GAMANAL and Peak Easy fits with correlated uncertainties. The Peak Easy results were 0.4% to 1.9% larger due to the differences in the peak fitting routine compared to GAMANAL. The measured activation products were used to scale the MC derived reactions to the experimental total fluence from the NIF source environment. The total fluence from the source was determined with χ^2 minimization and was 1.13×10^{16} neutrons.

The modeled results with MCNP5, including systematic uncertainty quantified with Sampler, show overall agreement with the exception of $^{58}Co^{g+m1}$, where including $^{58}Co^{g+m1}$ results in a χ^2/ν of 2.31 (p = 0.004). Similar research at the NIF has also found a suppression of nearly 27% production of $^{58}Co^{g+m1}$ (Bogetic, 2020). $^{58}Co^{g+m1}$ was removed from the unfolding dataset due to these inconsistencies; removing that reaction produces a χ^2/ν of 1.21 ($p = 0.267$). The $^{58}Co^{g+m1}$ product indicates either decreased neutron fluence over the reaction range or the reaction uncertainty was underestimated. There is some evidence to support this may be the case as the ENDF-B/VII.1 uncertainty for this reaction at 14 MeV is ~9x greater than the uncertainty in IRDFF-II, which was used in Sampler to obtain the integral uncertainty of 2.53%.

4.2. Unfolding

Table 4 summarizes the STAYSL changes to the ETA foil pack activation products following spectral adjustment and the individual χ^2 contributions. The neutron flux environment was constrained by the uncertainty and covariance matrix shown previously in Fig. 3. The resultant neutron fluence in the sample cavity was $1.49 \pm 0.01 \times 10^{12}$ neutrons cm^{-2}. ^{239}Np and ^{56}Mn had activation product changes of over 10%. ^{56}Mn was in a region of relatively large transport uncertainty as a thermal reaction but also has larger nuclear data uncertainty, reaching 24% at 0.125 MeV. Numerical precision, an inherent feature of the STAYSL code, was also a minor issue as noted in the negative χ^2 contribution for ^{89}Zr. The STAYSL-unfolded spectrum had a χ^2/ν = 1.62 (p = 0.071), which indicates that the modeled spectrum and covariance was in agreement with the experiment for these reaction products.

Table 4
STAYSL modifications to reaction products and χ^2 contributions.

Reaction Product	STAYSL Adjusted % Difference from Measured Reactions	χ^2 Contribution
$^{196}Au^{g+m1}$	0.74	0.08
^{198}Au	0.83	0.22
^{89}Zr	−0.09	−0.03
^{56}Mn	30.13	1.67
$^{116}In^{m1}$	−1.88	0.56
$^{116}In^{m1}$	4.66	0.61
$^{116}In^{m1}$	−5.20	2.59
^{239}Np	16.80	11.14
^{187}W	−1.22	0.10
^{57}Ni	−3.02	0.32
^{24}Na	−1.77	0.33
$^{196}Au^{g+m1}$	2.98	0.84
^{198}Au	0.34	0.05
χ^2/ν = 1.62 (p = 0.071)		

Neutron fluence results were compared though the Pearson correlation coefficient (PCC) and the Kolmogorov–Smirnov (K–S) statistic. The PCC metric, r, provides a measure of the linear relationship between two sets of data. The null hypothesis of the PCC is that there is no correlation between the two datasets. The p-value indicates the probability of an uncorrelated system producing a correlation coefficient at least as large in magnitude. Small p-values (<0.05) indicate a statistically significant PCC.

The K-S two-sample statistic, D, compares the cumulative distribution functions (CDF) between two sets of data. The K-S statistic provides information on the relative magnitude of the distributions and is calculated by the maximum difference between the expected and observed CDF. The null hypothesis for this test is that the two samples were drawn from the same distribution. Unlike the PCC, a large p-value (> 0.05) from the K-S statistic fails to reject the null hypothesis.

The STAYSL unfolded neutron spectrum is shown in Fig. 6. Activation ranges for several products overlap with the discarded $^{58}Co^{g+m1}$, most notably the threshold indium reactions. The modeled neutron

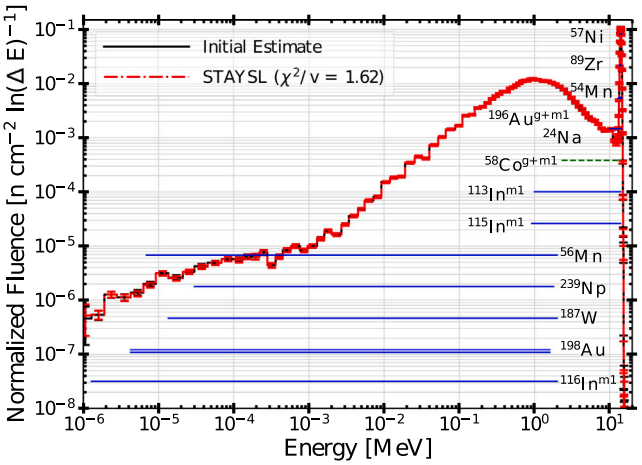

(a) Logarithmic energy scale

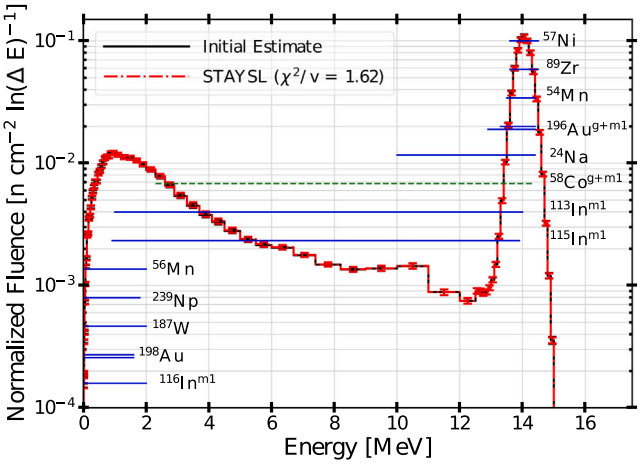

(b) Linear energy scale

Fig. 6. (Color online) Neutron fluence per unit lethargy for the initial guess and STAYSL unfolded result in (a) logarithmic energy scale and (b) linear energy scale. The horizontal lines indicate the 5%–95% activation ranges. The ^{58}Co^{g+m1} dotted horizontal line was not included in the unfold.

fluence was in agreement with the STAYSL unfolded results with $r = 1$ ($p \sim 0$) and $D = 0.04$ ($p = 1.00$), indicating that the Sampler methodology was representative of the neutron environment covariance matrix. The primary differences in the χ^2 values based on the MC models and STAYSL were the mismatch of group structures, representative environment in Sampler, use ENDF-B/VII.1 in Sampler transport, and numerical precision in STAYSL. Overall, the unfolded neutron spectrum indicates that the modeled neutron spectrum is in strong agreement with the experiment.

4.3. Fission products

The R_{97} distribution as a function of mass chain for cumulative yield fission products is shown in Fig. 7. The $N_i^{f,e} \Big/ N_{97}^{f,e}$ values for the distribution, including independent yields not graphed, are provided in Table 5 of the Appendix, along with the modeled neutron fluence in the HEU foils in Table 6. The modeled neutron fluence was used instead of the measured fluence due to the optical thickness of the foils resulting in non-negligible attenuation throughout the foil pack as shown in Fig. 5. Using the benchmarked model allowed the extraction of the fluence at the HEU foils thereby providing a more accurate assessment the neutron fluence seen by the HEU foils. The experimental

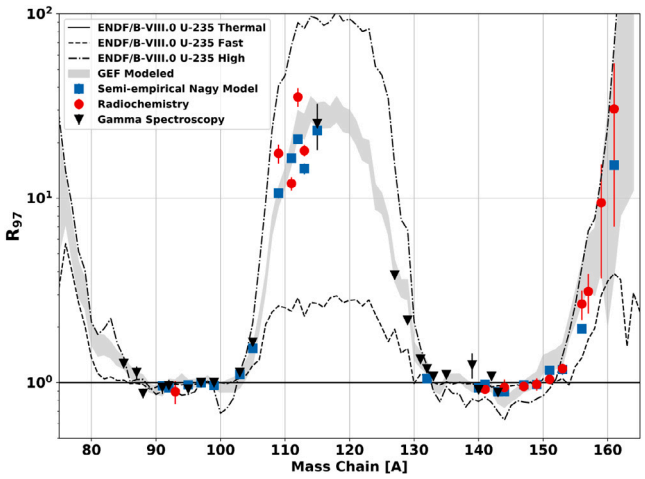

Fig. 7. (Color online) Comparison between the experimentally measured fission product yields and the modeled GEF and semi-empirical fit. ENDF-B/VIII.0 R values are provided as a reference.

measurements included 15 mass chains after radiochemical processing and 21 mass chain measurements by direct gamma spectrometry. The cadmium radiochemistry was not successful and was removed from solution with the precipitation of uranium hydroxide.

The results show moderate predictive capabilities to reproduce the experimental results. The χ^2/ν for the GEF and semi-empirical fits for the entire distribution were 1.58 and 2.50, respectively. The GEF results that contributed over 2.00 to the χ^2/ν were mass chains 88 (χ^2 = 3.5), 109 (9.1), 111 (4.3), 112 (2.8), 113 (2.7), 129 (6.0), 139 (2.3), 142 (5.2), and 144 (2.3). The semi-empirical fit results, which were only possible for mass chains with sufficient energy-dependent fission product yield data, that contributed more than 2.00 to the χ^2/ν were 109 (10.2), 111 (13.7), 112 (11.3), 113 (5.1), 151 (2.4), and 156 (2.0). The semi-empirical fits had similar performance to GEF. The missing correlation between the energy dependence of fission yields would improve the semi-empirical results if available.

The valley fission product mass chain region between $A = 109 - 113$ were inconsistent with the model. The peak fission products with an R value close to 1 were well modeled; however, the fission product yield is not highly energy dependent. There are several possible causes for the inability to accurately model mass chain fission product yields. First, there may be an unknown source of systematic uncertainty. Second and related to the radiochemically processed mass chains, the final solutions may contain precipitate particulates which would result in systematically biased recovery yield measurements. Third, recent publications have measured fission product yield as a function of energy that contradict current models for ^{235}U(n,f) Koehl et al. (2017) and ^{239}Pu(n,f) Gooden et al. (2016); therefore, more IFY experiments testing first- and second-chance fission models would be beneficial.

5. Conclusions

This work described the capability to modify the NIF D-T neutron spectrum to a moderated TN+PFNS. Customizable neutron spectra allow for increased access to study basic nuclear data such as integral fission product yields and dosimetry cross sections as well as develop integral benchmark experiments. The ETA experiment measured activation reaction products to quantify the experimental environment. IFY were obtained for neutron-induced fission of 93.215% ^{235}U HEU for 36 mass chains and include 47 independent and cumulative yields.

The neutron spectrum was modeled in MCNP5 using ENDF-B/VIII.0 and IRDFF-II nuclear data libraries. Systematic nuclear data uncertainties were calculated through stochastic sampling in SCALE Sampler

Table 5
Cumulative (C) and independent (I) $N_i^{f,e} \Big/ N_{97}^{f,e}$ HEU foil fission product values measured foil via gamma ray spectrometry (γ-spectrometry) or with prior radiochemical processing (RC).

Isotope	Measurement Type	Yield Type	$N_i^{f,e} \Big/ N_{97}^{f,e}$	% Error	Isotope	Measurement Type	Yield Type	$N_i^{f,e} \Big/ N_{97}^{f,e}$	% Error
Kr-85 m	γ-spectrometry	C	2.79E−01	3.9	I-132	γ-spectrometry	I	2.67E−02	15.8
Kr-87	γ-spectrometry	C	4.84E−01	7.2	I-133	γ-spectrometry	C	1.21E+00	4.2
Kr-88	γ-spectrometry	C	5.22E−01	5.7	I-135	γ-spectrometry	C	1.01E+00	3.0
Sr-91	γ-spectrometry	C	9.15E−01	7.5	Xe-135	γ-spectrometry	I	1.88E−01	5.4
Sr-92	γ-spectrometry	C	9.16E−01	6.9	Cs-136	γ-spectrometry	I	1.04E−02	25.4
Y-92	γ-spectrometry	I	5.20E−02	57.9	Ba-139	γ-spectrometry	C	1.33E+00	15.6
Y-93	γ-spectrometry	C	1.07E+00	14.2	Ba-140	γ-spectrometry	C	9.48E−01	3.4
Y-93	RC	C	9.46E−01	14.3	Ba-140	RC	C	1.03E+00	6.3
Zr-95	γ-spectrometry	C	1.00E+00	3.3	Ce-141	RC	C	8.96E−01	3.3
Zr-97	γ-spectrometry	C	1.00E+00	0.0	La-142	γ-spectrometry	C	1.06E+00	3.3
Mo-99	γ-spectrometry	C	1.02E+00	3.7	Ce-143	γ-spectrometry	C	8.78E−01	3.2
Ru-103	γ-spectrometry	C	5.75E−01	3.4	Ce-143	RC	C	8.56E−01	3.3
Rh-105	γ-spectrometry	C	2.71E−01	5.5	Ce-144	RC	C	8.65E−01	10.2
Ru-105	γ-spectrometry	C	2.66E−01	3.7	Nd-147	γ-spectrometry	C	3.56E−01	8.9
Pd-109	RC	C	9.11E−02	11.7	Nd-147	RC	C	3.57E−01	4.8
Ag-111	RC	C	3.49E−02	8.2	Pm-149	RC	C	1.77E−01	7.6
Pd-112	RC	C	7.71E−02	11.7	Pm-151	RC	C	7.28E−02	5.1
Ag-113	RC	C	4.29E−02	7.1	Sm-153	RC	C	3.15E−02	3.5
Cd-115	γ-spectrometry	C	5.32E−02	27.9	Sm-156	RC	C	6.61E−03	18.2
Sb-127	γ-spectrometry	C	1.00E−01	4.8	Eu-156	RC	C	3.78E−03	27.2
Sb-129	γ-spectrometry	C	1.97E−01	4.6	Eu-157	RC	C	3.21E−03	24.2
I-131	γ-spectrometry	C	5.37E−01	3.8	Gd-159	RC	C	1.59E−03	61.1
Te-131 m	γ-spectrometry	C	1.08E−01	8.4	Tb-161	RC	C	4.34E−04	77.1
Te-132	γ-spectrometry	C	8.29E−01	4.9					

Table 6
Energy distribution of neutron fluence in HEU sample.

Upper Energy [MeV]	n − cm^{-2}	Relative Error	Upper Energy [MeV]	n − cm^{-2}	Relative Error	Upper Energy [MeV]	n − cm^{-2}	Relative Error
1.00E−09	0.00E+00	21.34	1.90E−02	1.88E+09	0.04	7.40E+00	7.41E+09	0.05
1.00E−08	8.48E+03	7.91	2.55E−02	4.31E+09	0.04	8.20E+00	6.44E+09	0.06
2.30E−08	1.67E+05	7.25	3.20E−02	4.24E+09	0.03	9.00E+00	5.28E+09	0.08
5.00E−08	7.72E+05	4.69	4.00E−02	3.92E+09	0.03	1.00E+01	6.04E+09	0.09
7.60E−08	8.97E+05	3.12	5.25E−02	8.38E+09	0.03	1.10E+01	5.68E+09	0.08
1.15E−07	1.14E+06	2.83	6.60E−02	9.94E+09	0.03	1.20E+01	3.17E+09	0.07
1.70E−07	1.33E+06	2.02	8.80E−02	1.73E+10	0.03	1.25E+01	1.28E+09	0.06
2.55E−07	1.62E+06	1.10	1.10E−01	1.60E+10	0.03	1.26E+01	2.98E+08	0.06
3.80E−07	2.98E+06	0.94	1.35E−01	2.22E+10	0.03	1.27E+01	2.86E+08	0.06
5.50E−07	3.79E+06	1.20	1.60E−01	1.92E+10	0.03	1.28E+01	2.80E+08	0.06
8.40E−07	5.23E+06	0.64	1.90E−01	2.59E+10	0.03	1.29E+01	2.90E+08	0.06
1.28E−06	3.59E+06	1.11	2.20E−01	2.33E+10	0.03	1.30E+01	3.02E+08	0.06
1.90E−06	4.02E+06	0.51	2.55E−01	2.74E+10	0.03	1.31E+01	3.34E+08	0.05
2.80E−06	1.71E+07	0.20	2.90E−01	2.85E+10	0.03	1.32E+01	4.59E+08	0.05
4.25E−06	1.75E+07	0.19	3.20E−01	2.47E+10	0.03	1.33E+01	7.73E+08	0.05
6.30E−06	1.75E+07	0.28	3.60E−01	3.21E+10	0.03	1.34E+01	1.55E+09	0.05
9.20E−06	2.89E+07	0.18	4.00E−01	3.17E+10	0.03	1.35E+01	3.16E+09	0.05
1.35E−05	4.90E+07	0.14	4.50E−01	3.56E+10	0.03	1.36E+01	6.30E+09	0.05
2.10E−05	5.45E+07	0.17	5.00E−01	3.68E+10	0.03	1.37E+01	1.16E+10	0.05
3.00E−05	5.08E+07	0.12	5.50E−01	3.50E+10	0.03	1.38E+01	1.84E+10	0.05
4.50E−05	6.69E+07	0.14	6.00E−01	3.47E+10	0.03	1.39E+01	2.54E+10	0.05
6.90E−05	8.69E+07	0.12	6.60E−01	4.11E+10	0.03	1.40E+01	3.08E+10	0.05
1.00E−04	8.49E+07	0.13	7.20E−01	4.05E+10	0.03	1.41E+01	3.25E+10	0.04
1.35E−04	7.01E+07	0.15	7.80E−01	3.82E+10	0.03	1.42E+01	2.98E+10	0.04
1.70E−04	5.72E+07	0.14	8.40E−01	3.56E+10	0.03	1.43E+01	2.36E+10	0.04
2.20E−04	7.07E+07	0.21	9.20E−01	4.61E+10	0.03	1.44E+01	1.63E+10	0.05
2.80E−04	8.47E+07	0.22	1.00E+00	4.26E+10	0.03	1.45E+01	9.75E+09	0.05
3.60E−04	3.70E+07	0.20	1.20E+00	8.96E+10	0.03	1.46E+01	5.21E+09	0.05
4.50E−04	4.91E+07	0.20	1.40E+00	7.25E+10	0.03	1.47E+01	2.35E+09	0.05
5.75E−04	8.25E+07	0.19	1.60E+00	6.19E+10	0.03	1.48E+01	8.94E+08	0.05
7.60E−04	1.14E+08	0.16	1.80E+00	5.17E+10	0.03	1.49E+01	3.37E+08	0.06
9.60E−04	8.22E+07	0.13	2.00E+00	4.29E+10	0.03	1.50E+01	9.50E+07	0.09
1.28E−03	1.13E+08	0.10	2.30E+00	5.18E+10	0.03	1.51E+01	2.41E+07	0.16
1.60E−03	1.35E+08	0.09	2.60E+00	3.99E+10	0.03	1.52E+01	5.43E+06	0.30
2.00E−03	1.87E+08	0.08	2.90E+00	3.02E+10	0.04	1.53E+01	3.90E+06	0.51
2.70E−03	1.79E+08	0.09	3.30E+00	2.94E+10	0.04	1.54E+01	1.88E+05	0.87
3.40E−03	2.30E+08	0.10	3.70E+00	2.18E+10	0.05	1.55E+01	6.88E+03	1.00
4.50E−03	4.15E+08	0.09	4.10E+00	1.64E+10	0.05	1.56E+01	6.37E+04	0.68
5.50E−03	4.03E+08	0.09	4.50E+00	1.30E+10	0.05	1.57E+01	3.21E+04	0.73
7.20E−03	8.17E+08	0.08	5.00E+00	1.24E+10	0.05	1.58E+01	9.86E+03	1.00
9.20E−03	8.31E+08	0.06	5.50E+00	9.51E+09	0.04	1.59E+01	0.00E+00	0.06
1.20E−02	1.68E+09	0.05	6.00E+00	7.89E+09	0.04	1.60E+01	0.00E+00	0.06
1.50E−02	1.71E+09	0.05	6.70E+00	9.44E+09	0.04	1.65E+01	5.29E+04	1.00

using an ensemble of 285 realizations of the 252-group ENDF-B/VII.1 library. The CE MCNP5 mean results were used with the multi-group Sampler covariance results as an *a priori* guess spectrum for STAYSL to characterize the neutron flux in the ETA sample cavity with foil activation spectroscopy.

The 15 activation products produced in an activation foil pack were consistent with the model ($\chi^2/\nu = 1.21$) with the exception of $^{58}Co^{g+m1}$, which was excluded from the analysis due to large inconsistencies, which have been reported elsewhere for this reaction channel at NIF. The $^{58}Co^{g+m1}$ discrepancy will require additional research to resolve. The unfolded neutron spectrum was consistent with the model and passed statistical testing with $\chi^2/\nu = 1.62$ ($p = 0.071$). This indicates that the combination of MCNP5 and SCALE Sampler was adequate for the analysis; however, the model would benefit from improvements to the Sampler multi-group cross-section libraries for higher energy environments.

Fission product measurements indicate general agreement between the measurements and the models resulted from GEF and semi-empirical fits. However, silver and palladium valley fission products, along with several others, were not consistent and resulted in large individual χ^2 contributions. A repeated experiment and measurement of these mass chains would be ideal to provide benchmarks for model improvement. The semi-empirical fit performed worse than GEF; however, improvements can be made if fission product yield incident neutron energy correlations were available.

Future work aims to improve upon the ETA design to better match the NIF configuration constraints and increase the neutron fluence in the sample cavity. Additionally, $^{58}Co^{g+m1}$ measurements at NIF are planned to be taken under the D-T environment in addition to a similar moderated spectrum to further explore the large, yet consistent, discrepancies between modeled and experimental results at NIF.

CRediT authorship contribution statement

N. Quartemont: Conceptualization, Methodology, Software, Formal analysis, Investigation, Writing - original draft, Visualization. **N. Gharibyan:** Investigation, Data curation, Formal analysis, Writing - review & editing, Visualization. **K. Moody:** Investigation, Data curation, Formal analysis, Writing - review & editing, Visualization. **J.E. Bevins:** Supervision, Conceptualization, Project administration, Funding acquisition, Writing - review & editing.

Declaration of competing interest

The authors declare that they have no known competing financial interests or personal relationships that could have appeared to influence the work reported in this paper.

Acknowledgments

This research was supported in part by the U.S. Air Force Technical Application Center (AFTAC) under the AFIT/AFTAC Endowed Term Chair MOA#: 212196 and the Defense Threat Reduction Agency, USA under grant HDTRA-18-27434 and 19-29109. This work was performed under the auspices of the U.S. Department of Energy by Lawrence Livermore National Laboratory under Contract DE-AC52-07NA27344.

Additionally, the authors would like to thank Todd Woody, Keenan Thomas, Sam Glover, Brent Blue, and Charles Yeamans (Lawrence Livermore National Laboratory), Douglas Peplow and William Wieselquist (Oak Ridge National Laboratory), Larry Greenwood (Pacific Northwest National Laboratory), and Glenn Sjoden (Air Force Technical Applications Center) for their invaluable support of this research.

Appendix. Measured $N_i^{f,e} \Big/ N_{97}^{f,e}$ values and neutron environment

Table 5 provides the $N_i^{f,e} \Big/ N_{97}^{f,e}$ values measured for the ETA experiment based on a measured 2.90E+08 ± 2.1% ^{97}Zr atoms per gram of HEU sample. The associated modeled HEU neutron fluence in the STAYSL 129-group structure is shown in Table 6. Mass chain yields for A of 92, 131, 132, and 135 were calculated as the sum of both fission products in the respective mass chains. Fission products uncertainty includes nuclear data uncertainty, counting statistics, chemical recovery uncertainty, and weighted averaging for repeated measurements. Large uncertainties above $A = 156$ are primarily due to counting statistics.

References

Appelbe, B., Chittenden, J., 2014. Relativistically correct DD and DT neutron spectra. High Energy Density Phys. 11 (1), 30–35. http://dx.doi.org/10.1016/j.hedp.2014.01.003.

Basunia, M.S., 2009. Nuclear data sheets for A = 187. Nucl. Data Sheets 110 (5), 999–1238. http://dx.doi.org/10.1016/j.nds.2009.04.001.

Bernstein, L.A., Brown, D.A., Koning, A.J., Rearden, B.T., Romano, C.E., Sonzogni, A.A., Voyles, A.S., Younes, W., 2019. Our future nuclear data needs. Annu. Rev. Nucl. Part. Sci. 69 (109), http://dx.doi.org/10.1146/annurev-nucl-101918-023708.

Bevins, J., 2017. Targeted Modification of Neutron Energy Spectra for National Security Applications (Ph.D. thesis). University of California, Berkeley.

Bevins, J.E., Sweger, Z., Munshi, N., Goldblum, B., Brown, J., Bleuel, D., Bernstein, L., Slaybaugh, R., 2019. Performance evaluation of an energy tuning assembly for neutron spectral shaping. Nucl. Instrum. Methods Phys. Res. A 923, 79–87. http://dx.doi.org/10.1016/j.nima.2019.01.049.

Bhat, M.R., 1998. Nuclear data sheets for A = 57. Nucl. Data Sheets 85, 415–536. http://dx.doi.org/10.1016/j.ssc.2010.07.050.

Blachot, J., 2010a. Nuclear data sheets for A = 113. Nucl. Data Sheets 111, 1471–1618. http://dx.doi.org/10.1016/j.nds.2010.05.001.

Blachot, J., 2010b. Nuclear data sheets for A = 116. Nucl. Data Sheets 111, 717–895. http://dx.doi.org/10.1016/j.nds.2010.03.002.

Blachot, J., 2012. Nuclear data sheets for A = 115. Nucl. Data Sheets 113, 2391–2535. http://dx.doi.org/10.1016/j.nds.2012.10.002.

Bogetic, S., 2020. Improvements, Validation, and Applications of a Metaheuristic Optimization Method for Neutron Spectra Tailoring at the National Ignition Facility (Ph.D. thesis). University of California, Berkeley, http://dx.doi.org/10.2172/1631912.

Brown, D., et al., 2018. ENDF/B-VIII.0: The 8th major release of the nuclear reaction data library with CIELO-project cross sections, new standards and thermal scattering data. Nucl. Data Sheets 148, 1–142. http://dx.doi.org/10.1016/j.nds.2018.02.001, URL: http://www.sciencedirect.com/science/article/pii/S0090375218300206, Special Issue on Nuclear Reaction Data.

Browne, E., Tuli, J.K., 2015. Nuclear data sheets for A = 238. Nucl. Data Sheets 127, 191–332. http://dx.doi.org/10.1016/j.nds.2015.07.003.

Chadwick, M., et al., 2011. ENDF/B-VII.1 Nuclear data for science and technology: Cross sections, covariances, fission product yield. Nucl. Data Sheets 112 (12), 2887–2996. http://dx.doi.org/10.1016/j.nds.2011.11.002.

DeVoe, J.R., 1960. The Radiochemistry of Cadmium, Nuclear Science Series (National Research Council (U.S.)); No. 3001. NAS-NS-3001, Technical Report, Subcommittee on Radiochemistry, National Academy of Sciences-National Research Council; available from the Office of Technical Services, Dept. of Commerce, available from the Office of Technical Services, Dept. of Commerce, National Academy of Sciences, Washington, D.C.

Dong, Y., Junde, H., 2014. Nuclear data sheets for A = 54. Nucl. Data Sheets 121, 1–142. http://dx.doi.org/10.1016/j.nds.2014.09.001.

Ellison, C.L., et al., 2018. Development and modeling of a polar-direct-drive exploding pusher platform at the national ignition facility. Phys. Plasmas 25 (7), http://dx.doi.org/10.1063/1.5025724.

Faris, J.P., Warton, J.W., 1962. Anion exchange resin separation of the rare earths, yttrium, and scandium in nitric acid-methanol mixtures. Anal. Chem. 34 (9), 1077–1080. http://dx.doi.org/10.1021/ac60189a013.

Firestone, R., 1996. Table of Isotopes. John Wiley & Sons, New York, NY.

Firestone, R.B., 2007. Nuclear data sheets for A = 24. Nucl. Data Sheets 108, 2319–2392. http://dx.doi.org/10.1016/j.nds.2007.10.001.

Gharibyan, N., Moody, K.J., Despotopulos, J.D., Grant, P.M., Shaughnessy, D.A., 2015. First fission yield measurements at the national ignition facility: 14-MeV neutron fission of 238U. J. Radioanal. Nucl. Chem. 303 (2), 1335–1338. http://dx.doi.org/10.1007/s10967-014-3474-6.

Gharibyan, N., Moody, K., Tumey, S., Brown, T., Grant, P., Bench, G., Shaughnessy, D., 2018. Development of a "Fission-proxy" method for the measurement of 14-MeV neutron fission yields. Radiochim. Acta 106 (8), 627–630. http://dx.doi.org/10.1515/ract-2017-2889.

Gooden, M.E., et al., 2016. Energy dependence of fission product yields from ^{235}U, ^{238}U and ^{239}Pu for incident neutron energies between 0.5 and 14.8 MeV. Nucl. Data Sheets 131, 319–356. http://dx.doi.org/10.1016/j.nds.2015.12.006.

Greenwood, L., Johnson, C., 2016. Least-squares neutron spectral adjustment with STAYSL PNNL. EPJ Web Conf. 106, 07001. http://dx.doi.org/10.1051/epjconf/201610607001.

Gunnink, R., Niday, J.B., 1972. Computerized Quantitative Analysis By Gamma-Ray Spectrometry. Vol. 1. Description of the Gamanal Program. Technical Report, Lawrence Livermore Laboratory, Livermore, CA, http://dx.doi.org/10.2172/4696896.

Hogdahl, O.T., 1961. Radiochemistry of Palladium, Nuclear Science Series (National Research Council (U.S.)); No. 3052. NAS-NS-3052, Technical Report, National Academy of Sciences - National Research Council.

Huang, X., Kang, M., 2016. Nuclear data sheets for A = 198. Nucl. Data Sheets 133, 221–416. http://dx.doi.org/10.1016/j.nds.2016.02.002.

Junde, H., Su, H., Dong, Y., 2011. Nuclear data sheets for A = 56. Nucl. Data Sheets 112, 1513–1645. http://dx.doi.org/10.1016/j.nds.2011.04.004.

Kahler, A.C., MacFarlane, R.E., Chadwick, M.B., 2014. Integral data testing of ENDF/B-VII.1 files - success stories and need to improve stories. Nucl. Data Sheets 118 (1), 410–413. http://dx.doi.org/10.1016/j.nds.2014.04.093.

Koehl, M.A., Rundberg, R.S., Shafer, J.C., 2017. Relative fission product yields in the USGS TRIGA MARK I reactor. J. Radioanal. Nucl. Chem. 314 (2), 1375–1381. http://dx.doi.org/10.1007/s10967-017-5485-6.

Moody, K.J., Gharibyan, N., Shaughnessy, D.A., Grant, P.M., Gostic, J.M., Cerjan, C.J., Yeamans, C.B., Despotopulos, J.D., Faye, S.A., 2020. Nuclear spectrometry of 9.6 h ^{196}Au^{m2} and the reaction of ^{197}Au with fast neutrons. J. Phys. G: Nucl. Part. Phys. 47 (4), 1–48. http://dx.doi.org/10.1088/1361-6471/ab67e9.

Nagy, S., Flynn, K.F., Gindler, J.E., Meadows, J.W., Glendenin, L.E., 1978. Mass distributions in monoenergetic-neutron-induced fission of ^{238}U. Phys. Rev. C 17 (1), 163–171. http://dx.doi.org/10.1103/PhysRevC.17.163.

Nesaraja, C.D., Geraedts, S.D., Singh, B., 2010. Nuclear data sheets for A = 58. Nucl. Data Sheets 111, 897–1092. http://dx.doi.org/10.1016/j.nds.2010.03.003.

Perey, F.G., 1977. Least-Squares Dosimetry Unfolding: The Program STAY'SL (ORNL/TM-6062). Oak Ridge National Laboratory, Oak Ridge, Tennessee.

Quartemont, N.J., 2021. NIF ETA Experiment. Mendeley Data, http://dx.doi.org/10.17632/92n6k43nt5.2.

Quartemont, N.J., Bevins, J.E., Slaybaugh, R., Bernstein, L., 2020a. Analysis of an energy tuning assembly for simulating nuclear weapon environments at the national ignition facility. J. Radiat. Effects Res. Eng. 38, arXiv:https://apps.dtic.mil/sti/pdfs/AD1093191.pdf.

Quartemont, N.J., Bickley, A.A., Bevins, J.E., 2020b. Nuclear data covariance analysis in radiation transport simulations utilizing SCALE sampler and the IRDFF nuclear data library. IEEE Trans. Nucl. Sci. 67 (3), 482–491. http://dx.doi.org/10.1109/TNS.2020.2970700.

Rearden, B., Jessee, M. (Eds.), 2013. User Guide for the STAYSL PNNL Suite of Software Tools, PNNL-22253. Pacific Northwest National Laboratory, Richland, WA, http://dx.doi.org/10.2172/1067961.

Rearden, B., Jessee, M. (Eds.), 2018. SCALE Code System, ORNL/TM-2005/39, Version 6.2.3, Technical Report. Oak Ridge National Laboratory, Oak Ridge, Tennessee, http://dx.doi.org/10.2172/1426571.

Schmidt, K.H., Jurado, B., Amouroux, C., Schmitt, C., 2016. General description of fission observables: GEF model code. Nucl. Data Sheets 131, 107–221. http://dx.doi.org/10.1016/j.nds.2015.12.009.

Selby, H., Mac Innes, M., Barr, D., Keksis, A., Meade, R., Burns, C., Chadwick, M., Wallstrom, T., 2010. Fission product data measured at los alamos for fission spectrum and thermal neutrons on ^{239}Pu, ^{235}U, ^{238}U. Nucl. Data Sheets 111 (12), 2891–2922. http://dx.doi.org/10.1016/j.nds.2010.11.002, URL: http://www.sciencedirect.com/science/article/pii/S0090375210001018.

Singh, B., 2013. Nuclear data sheets for A = 89. Nucl. Data Sheets 114, 1–208. http://dx.doi.org/10.1016/j.nds.2013.01.001.

Sunderman, D.N., Townley, C.W., 1961. Radiochemistry of Silver, Nuclear Science Series (National Research Council (U.S.)); No. 3047. NAS-NS-3047, Technical Report, National Academy of Sciences-National Research Council, U.S. Atomic Energy Commission; available from the Office of Technical Services, Dept. of Commerce, National Academy of Sciences.

Taavitsainen, A., Vanhanen, R., 2017. On the maximum entropy distributions of inherently positive nuclear data. Nucl. Instrum. Methods Phys. Res. A 854 (November 2016), 156–162. http://dx.doi.org/10.1016/j.nima.2016.11.061.

Trkov, A., et al., 2020. IRDFF-II: A new neutron metrology library. Nucl. Data Sheets 163, 1–108, arXiv:https://arxiv.org/abs/1909.03336v2.

Vagena, E., Theodorou, K., Stoulos, S., 2018. Thick-foils activation technique for neutron spectrum unfolding with the MINUIT routine—Comparison with GEANT4 simulations. Nucl. Instrum. Methods Phys. Res. A 887 (January), 64–69. http://dx.doi.org/10.1016/j.nima.2018.01.025.

X-5 Monte Carlo Team, 2008. MCNP - A general Monte Carlo N-particle transport code, version 5, LA-UR-03-1987.

Xiaolong, H., 2007. Nuclear data sheets for A = 196. Nucl. Data Sheets 108, 1093–1286. http://dx.doi.org/10.1016/j.nds.2007.05.001.

Yeamans, C.B., Bleuel, D.L., 2017. The spatially distributed neutron activation diagnostic FNADs at the national ignition facility. Fusion Sci. Technol. 72 (2), 120–128. http://dx.doi.org/10.1080/15361055.2017.1320499.